



Improved Delayed Detached Eddy Simulation of AGARD Wing Flutter with Fully Coupled Fluid-Structure Interaction

Purvic Patel* and Gecheng Zha†
Dept. of Mechanical and Aerospace Engineering
University of Miami, Coral Gables, Florida 33124
E-mail: gzha@miami.edu

The Shear Stress Transport model based improved delayed detached eddy simulation of the AGARD Wing 445.6 is performed at the subsonic, transonic and supersonic flow with high order shock capturing schemes. An implicit unfactored Gauss-Seidel line iteration scheme is used to solve the compressible, filtered Navier-Stokes equations. The flow solver and the modal form structural solver utilize the dual time-stepping scheme to achieve fully coupled fluid-structural interaction via successive iterations using a pseudo time step. The LES sub-grid length scale based on the vorticity aligned with a grid line is used to overcome the standard sub-grid length scale's delayed flow transition problem. The predicted flutter boundary agrees well with the experiment at different Mach numbers, including the supersonic flow where the traditional RANS methods over-predict the flutter velocity index and frequency. At the transonic and supersonic flow, the torsional mode generalized displacement is decreased due to the shock oscillations over the suction and pressure surface of the wing. At the flutter boundary, no flow separation is observed at different Mach numbers.

I. Nomenclature

L_∞	=	Reference length
ρ_∞	=	free stream density
U_∞	=	free stream velocity
μ_∞	=	free stream dynamics viscosity
c_∞	=	free stream speed of sound
M_∞	=	free stream Mach number
d	=	Distance from the nearest wall
Ω	=	Vorticity magnitude
S	=	Strain rate magnitude
Pr	=	Prandtl number
Re	=	Reynolds number
i, j, k	=	Dummy indices for Indicial/Einstein summation notation
κ	=	von Karmann constant
δ_{ij}	=	Kronecker delta
Δt	=	Physical time step
U, V, W	=	Contravariant velocities in ξ, η and ζ directions
k	=	Turbulence kinetic energy (k)
ω	=	Turbulence specific dissipation rate (ω)

II. Introduction

Aeroelasticity is the science of studying the combined effect of inertia, elastic and aerodynamic forces on the flexible body due to the surrounding fluid's relative motion. Modern high-speed aircraft is made of thin, flexible structures to reduce the wave drag and its overall weight. These flexible wing structures are subjected to various loading conditions

*Ph.D. Candidate

†Professor, ASME Fellow, AIAA associate Fellow.

during the entire flight envelope and maneuvering. Therefore, their aeroelastic analysis is vital from the design phase to reduce later design modifications and experimental tests.

In the case of self-excited vibration (i.e., flutter), the aircraft wing vibrates at a natural frequency due to flow instabilities generated by the vibrating wing. The aerodynamic force feeds energy to the wing structure with each vibration cycle. With the insufficient overall damping, the amplitude of vibration increases with cycle and the wing structure integrity is eventually compromised, leading to the catastrophic outcome. At the flutter boundary, the wing experiences Limit-Cycle Oscillation (LCO), which can lead to the wing's fatigue failure. Below the flutter boundary, the vibrations are damped out.

The wing flutter boundary is a function of the flight Mach number, mass ratio and the angle-of-attack. Dynamic pressure at flutter decreases with increasing Mach number to the lowest value in the transonic flow regime [1]. This transonic dip is associated with the inherent non-linear flow features like shock waves, boundary layer, etc. [2] leading to non-linear wing response, which linear perturbation theory fails to predict accurately. The severity of the flutter boundary dip prediction is vital for safe flying conditions. The linear analysis adequately predicts the flutter boundary in the subsonic and supersonic flow [3]. However, the over-prediction of the flutter boundary increases with the increasing supersonic flow Mach number. The inclusion of the viscosity effect improves the flutter boundary prediction at the supersonic flow, where structural damping and number of structural modes have a lesser effect [4].

The Flutter characteristics of the AGARD standard aeroelastic wing case, Wing 445.6, has been studied by many researchers using different approaches over the years. Cunningham et al. [5] used the transonic small disturbance equation and the full potential equation to investigate the flutter characteristics of the AGARD Wing 445.6. Rausch et al. [6] and Lee-Rausch et al. [7] used the Euler equations to compute the complete flutter boundary. Their results show good agreement with the experimental results below free stream Mach number of one and a sudden rise in the flutter boundary above one. A later study by Lee-Rausch et al. [4] shows that the viscosity inclusion delays the rise in the flutter boundary on the supersonic side and thereby improves the prediction. Opgenoord [8] attributes the transonic flutter dip to the phase lag aerodynamic response. This lagged response is the effect of lagged information travel between the point near the leading and trailing edge of a wing in the presence of supersonic flow region between them.

In the time-marching Navier-Stokes solver, Reynolds-Averaged Navier-Stokes (RANS) equations are often solved to predict and include the viscosity effect. The compressible RANS approach is widely used for the compressible attached flow simulation due to its superiority in terms of computational cost and storage requirements in comparison to Direct Numerical Simulation (DNS) or Large Eddy Simulation (LES) [9]. However, their underlying feature of modeling the entire turbulence spectrum adversely affects their accuracy for the flow involving boundary layer separation, shock-wave boundary layer interaction, etc. On the other hand, LES resolves a large portion of the turbulence spectrum representing the large energy-containing eddies and models the effect of small isotropic eddies. However, their high computational cost impedes the use of LES for high Reynolds number industrial applications.

In the hybrid RANS/LES approach, the RANS is used to model the boundary layer, whereas the LES is used outside the boundary layer. Therefore, it combines the advantages of both approaches in terms of resolving large energy-containing eddies with the LES and reducing the computational cost by modeling the boundary layer with the RANS. In 1997, Spalart et al. [10] proposed the first Detached Eddy Simulation based on the one-equation Spalart-Allmaras (SA) model, commonly referred as DES97. The DES97 model switches from RANS to LES based on the local grid step size. This explicit switch causes the Grid Induced Separation under the extreme case of Modeled Stress Depletion (MSD) [11, 12]. To overcome DES97's Modeled Stress Depletion (MSD) problem, Strelets [13] and Menter et al. [14] proposed a zonal DES formulation based on the two-equation Shear Stress Transport (SST) model by shielding the boundary layer from the DES limiter. Spalart et al. [12] later proposed non-zonal Delayed Detached Eddy Simulation (DDES) deriving an idea of shielding the boundary layer from Menter et al. [14]. Their shielding function formulation depends on the eddy viscosity and the nearest wall distance and it can be used with any turbulence model involving eddy viscosity. Nikitin et al. [15] observed mismatch between modeled and resolved log layer, termed as Log Layer Mismatch (LLM), with the use of DES97 for wall-modeling in LES (WMLES) in the planar channel flow. Later, Shur et al. [16] proposed the Improved Delayed Detached Eddy Simulation (IDDES) aimed at wall modeling in the LES (WMLES) and it also addresses the LLM and MSD problem faced by the DES97 and DDES. Gritskevich et al. [17] revisited and recalibrated the shielding functions of DDES and IDDES models combined with the SST turbulence model.

The non-zonal DES and DDES based hybrid RANS/LES model suffers from the Grey Area (GA) problem, i.e., the transition region between the RANS and LES model. The length and extent of this region is the case and numerical scheme sensitive, in addition to the underlying RANS model [13, 18–21]. To mitigate this problem, various hybrid models are developed along with different LES filter width and other techniques like Synthetic Turbulence Generator

(STG). In the present study, the vorticity aligned with a grid line based on Chauvet et al. [22] is used with the SST-IDDES model to mitigate the GA problem of the standard LES sub-grid length scale based on Δ_{max} .

Chen et al. [23], Im et al. [24] and Gan et al. [25] have investigated the AGARD Wing 445.6 flutter boundary using the DDES based on the SA model. They have used the low diffusion, high-order shock-capturing 5th order Weighted Essentially Non-Oscillatory (WENO) scheme for inviscid fluxes. Their results have shown accurate prediction of the flutter boundary at transonic and supersonic flow for the first time. Šekutkovski et al. [26] have proposed and applied Scale-Adaptive Improved Delayed Detached Eddy Simulation based on the SST model (i.e. $k - \omega$ SST SA IDDES) to AGARD 445.6 wing flutter boundary prediction. Their results agree well at the supersonic flow. In contrast, the flutter boundary is over-predicted by more than 7% and 10% at transonic and subsonic flow, respectively. It is similar to the SST and SA model prediction.

The purpose of this paper is to calculate the AGARD wing flutter boundary using higher-order schemes and SST-IDDES [27] with a fully coupled FSI simulation to examine the robustness and accuracy of the methodology. This is an important step to advance the high fidelity hybrid RANS/LES methodology to the challenging aeroelasticity field, which often involves complex shock boundary layer interaction and vortical flows. The Roe's approximate Riemann solver is used to calculate the inviscid flux with the 5th order WENO scheme and the 4th order central differencing scheme for the viscous flux. The predicted flutter boundary agrees well with the experiment.

III. Numerical Model for Flow

The unsteady, Favre-filtered, compressible Navier-Stokes equations can be written in the nondimensional form using the generalized coordinates (ξ, η, ζ) as:

$$\frac{\partial \mathbf{Q}}{\partial t} + \frac{\partial \mathbf{E}}{\partial \xi} + \frac{\partial \mathbf{F}}{\partial \eta} + \frac{\partial \mathbf{G}}{\partial \zeta} = \frac{1}{Re} \left(\frac{\partial \mathbf{R}}{\partial \xi} + \frac{\partial \mathbf{S}}{\partial \eta} + \frac{\partial \mathbf{T}}{\partial \zeta} \right) \quad (1)$$

where, Re is the Reynolds number. The equations are normalized using the reference length (L_∞), free stream density (ρ_∞), velocity (U_∞) and dynamic viscosity (μ_∞). The conservative variable vector \mathbf{Q} and inviscid flux vectors \mathbf{E} , \mathbf{F} , \mathbf{G} and viscous flux vectors \mathbf{R} , \mathbf{S} , \mathbf{T} through the cell interface with the normal in the positive ξ , η , ζ direction, respectively are expressed as:

$$\mathbf{Q} = \frac{1}{J} \begin{pmatrix} \bar{\rho} \\ \bar{\rho}\tilde{u} \\ \bar{\rho}\tilde{v} \\ \bar{\rho}\tilde{w} \\ \bar{\rho}\tilde{e} \end{pmatrix}, \mathbf{E} = \begin{pmatrix} \bar{\rho}U \\ \bar{\rho}\tilde{u}U + l_x\bar{p} \\ \bar{\rho}\tilde{v}U + l_y\bar{p} \\ \bar{\rho}\tilde{w}U + l_z\bar{p} \\ (\bar{\rho}\tilde{e} + \bar{p})U - l_t\bar{p} \end{pmatrix}, \mathbf{F} = \begin{pmatrix} \bar{\rho}V \\ \bar{\rho}\tilde{u}V + m_x\bar{p} \\ \bar{\rho}\tilde{v}V + m_y\bar{p} \\ \bar{\rho}\tilde{w}V + m_z\bar{p} \\ (\bar{\rho}\tilde{e} + \bar{p})V - m_t\bar{p} \end{pmatrix}, \mathbf{G} = \begin{pmatrix} \bar{\rho}W \\ \bar{\rho}\tilde{u}W + n_x\bar{p} \\ \bar{\rho}\tilde{v}W + n_y\bar{p} \\ \bar{\rho}\tilde{w}W + n_z\bar{p} \\ (\bar{\rho}\tilde{e} + \bar{p})W - n_t\bar{p} \end{pmatrix} \quad (2)$$

$$\mathbf{R} = \begin{pmatrix} 0 \\ l_k\tilde{\tau}_{xk} \\ l_k\tilde{\tau}_{yk} \\ l_k\tilde{\tau}_{zk} \\ l_k(\tilde{u}_i\tilde{\tau}_{ki} + \tilde{q}_k) \end{pmatrix}, \mathbf{S} = \begin{pmatrix} 0 \\ m_k\tilde{\tau}_{xk} \\ m_k\tilde{\tau}_{yk} \\ m_k\tilde{\tau}_{zk} \\ m_k(\tilde{u}_i\tilde{\tau}_{ki} + \tilde{q}_k) \end{pmatrix}, \mathbf{T} = \begin{pmatrix} 0 \\ n_k\tilde{\tau}_{xk} \\ n_k\tilde{\tau}_{yk} \\ n_k\tilde{\tau}_{zk} \\ n_k(\tilde{u}_i\tilde{\tau}_{ki} + \tilde{q}_k) \end{pmatrix} \quad (3)$$

where J is the coordinate transformation Jacobian, ρ is the density, p is the static pressure and e is the total internal energy per unit mass. The overbar denotes Reynolds averaged and tilde represents the Favre filtered variable. The contravariant velocities (Eq. (4)) through each cell interface are defined as:

$$\begin{aligned} U &= l_t + \mathbf{l} \cdot \mathbf{V} = l_t + l_x\tilde{u} + l_y\tilde{v} + l_z\tilde{w} \\ V &= m_t + \mathbf{m} \cdot \mathbf{V} = m_t + m_x\tilde{u} + m_y\tilde{v} + m_z\tilde{w} \\ W &= n_t + \mathbf{n} \cdot \mathbf{V} = n_t + n_x\tilde{u} + n_y\tilde{v} + n_z\tilde{w} \end{aligned} \quad (4)$$

where, \mathbf{l} , \mathbf{m} , \mathbf{n} represent the normal vectors with their magnitudes equal to the elemental surface areas and pointing in the positive ξ , η , ζ directions respectively. These vectors are calculated at the cell interface center and written as:

$$\mathbf{l} = \frac{\nabla\xi}{J}, \mathbf{m} = \frac{\nabla\eta}{J}, \mathbf{n} = \frac{\nabla\zeta}{J} \quad (5)$$

and the grid moving velocities are defined as,

$$l_t = \frac{\xi_t}{J}, \quad m_t = \frac{\eta_t}{J}, \quad n_t = \frac{\zeta_t}{J} \quad (6)$$

Let the subscripts i, j, k represent the coordinates x, y, z . Using the Einstein summation convention, the total shear stress ($\tilde{\tau}_{ik}$) and the total heat flux (\tilde{q}_j) for turbulent flow are given by:

$$\begin{aligned} \tilde{\tau}_{ik} &= (\mu + \mu_{IDDES}) \left[\left(\frac{\partial \tilde{u}_i}{\partial x_k} + \frac{\partial \tilde{u}_k}{\partial x_i} \right) - \frac{2}{3} \delta_{ik} \frac{\partial \tilde{u}_j}{\partial x_j} \right] - \frac{2}{3} \delta_{ik} \bar{\rho} \tilde{k} Re \\ \tilde{q}_j &= -\frac{1}{(\gamma - 1) M_\infty^2} \left(\frac{\mu}{Pr} + \frac{\mu_{IDDES}}{Pr_t} \right) \frac{\partial \tilde{T}}{\partial x_j} \end{aligned} \quad (7)$$

where, μ is the molecular viscosity, M_∞ is the free stream Mach number. The molecular viscosity is determined using Sutherland's law. The turbulent viscosity μ_{IDDES} is computed based on the SST-IDDES turbulence model explained in the following section. The equation of state relating the dimensionless density, pressure and temperature is given as,

$$\bar{\rho} \tilde{e} = \frac{\bar{P}}{\gamma - 1} + \frac{1}{2} \bar{\rho} (\tilde{u}^2 + \tilde{v}^2 + \tilde{w}^2) + \bar{\rho} \tilde{k} \quad (8)$$

For the simplicity, all the bar and tilde in above equations will be dropped in the rest of this paper.

A. Improved Delayed Detached Eddy Simulation (IDDES)

Gritskevich et al. [17] proposed an advanced hybrid RANS/LES turbulence, the improved delayed detached eddy simulation based on the Shear Stress Transport (SST) model. The model solves two additional transport equations, i.e., for the turbulence kinetic energy (k) and the turbulence specific dissipation rate (ω), to calculate the eddy viscosity (μ_{IDDES}). In the generalized coordinates, the nondimensional conservative form of the SST-IDDES model's transport equations are given by:

$$\begin{aligned} \frac{\partial \frac{1}{J} \rho k}{\partial t} + \frac{\partial \rho k U}{\partial \xi} + \frac{\partial \rho k V}{\partial \eta} + \frac{\partial \rho k W}{\partial \zeta} &= \frac{1}{Re} \left[\frac{\partial}{\partial \xi} ((\mu + \sigma_k \mu_{IDDES}) (\mathbf{l} \cdot \nabla k)) \right. \\ &+ \frac{\partial}{\partial \eta} ((\mu + \sigma_k \mu_{IDDES}) (\mathbf{m} \cdot \nabla k)) + \frac{\partial}{\partial \zeta} ((\mu + \sigma_k \mu_{IDDES}) (\mathbf{n} \cdot \nabla k)) \left. \right] \\ &+ \tilde{P}_k - \rho \sqrt{k^3} / l_{IDDES} \end{aligned} \quad (9)$$

$$\begin{aligned} \frac{\partial \frac{1}{J} \rho \omega}{\partial t} + \frac{\partial \rho \omega U}{\partial \xi} + \frac{\partial \rho \omega V}{\partial \eta} + \frac{\partial \rho \omega W}{\partial \zeta} &= \frac{1}{Re} \left[\frac{\partial}{\partial \xi} ((\mu + \sigma_\omega \mu_{IDDES}) (\mathbf{l} \cdot \nabla \omega)) \right. \\ &+ \frac{\partial}{\partial \eta} ((\mu + \sigma_\omega \mu_{IDDES}) (\mathbf{m} \cdot \nabla \omega)) + \frac{\partial}{\partial \zeta} ((\mu + \sigma_\omega \mu_{IDDES}) (\mathbf{n} \cdot \nabla \omega)) \left. \right] \\ &+ P_\omega - \beta \rho \omega^2 + 2(1 - F_1) \frac{\rho \sigma_\omega}{\omega} \frac{\partial k}{\partial x_j} \frac{\partial \omega}{\partial x_j} \end{aligned} \quad (10)$$

The production limiter is used to avoid the turbulence built-up in the stagnation regions. The production term of turbulence kinetic energy and turbulent specific dissipation rate is given by:

$$\begin{aligned} P_k &= \frac{1}{Re} \left[\mu_t \left(\frac{\partial u_i}{\partial x_j} + \frac{\partial u_j}{\partial x_i} - \frac{2}{3} \delta_{ij} \frac{\partial u_k}{\partial x_k} \right) - \frac{2}{3} \rho k \delta_{ij} Re \right] \frac{\partial u_i}{\partial x_j} \\ \tilde{P}_k &= \min(P_k, 10\beta^* \rho \omega k) \\ P_\omega &= \frac{\rho \gamma}{\mu_t} \tilde{P}_k Re \end{aligned} \quad (11)$$

The turbulent viscosity (μ_{IDDES}) is calculated by:

$$\mu_{IDDES} = \frac{\rho a_1 k}{\max(a_1 \omega, SF_2)} Re, \quad S = \sqrt{S_{ij} S_{ij}}, \quad S_{ij} = \frac{1}{2} \left(\frac{\partial u_i}{\partial x_j} + \frac{\partial u_j}{\partial x_i} \right) \quad (12)$$

The blending functions F_1 and F_2 are given by:

$$\begin{aligned}
F_1 &= \tanh\left(\text{arg}_1^4\right) \\
F_2 &= \tanh\left(\text{arg}_2^2\right) \\
\text{arg}_1 &= \min\left[\max\left(\frac{\sqrt{k}}{\beta^*\omega d}, \frac{500\mu}{\rho d^2\omega} \frac{1}{Re}\right), \frac{4\rho k\sigma_{\omega 2}}{CD_{k\omega}d^2}\right] \\
\text{arg}_2 &= \max\left(\frac{2\sqrt{k}}{\beta^*\omega d}, \frac{500\mu}{\rho d^2\omega} \frac{1}{Re}\right)
\end{aligned} \tag{13}$$

The SST model coefficients are blended by:

$$\begin{aligned}
\sigma_k &= F_1\sigma_{k1} + (1 - F_1)\sigma_{k2}, & \sigma_{\omega} &= F_1\sigma_{\omega 1} + (1 - F_1)\sigma_{\omega 2} \\
\gamma &= F_1\gamma_1 + (1 - F_1)\gamma_2, & \beta &= F_1\beta_1 + (1 - F_1)\beta_2
\end{aligned} \tag{14}$$

Closure coefficients:

$$\begin{aligned}
\beta^* &= 0.09, & \sigma_{k1} &= 0.85, & \sigma_{k2} &= 1.0, & \beta_1 &= 0.075, & \beta_2 &= 0.0828 \\
\sigma_{\omega 1} &= 0.5, & \sigma_{\omega 2} &= 0.856, & \gamma_1 &= \frac{5}{9}, & \gamma_2 &= 0.44, & a_1 &= 0.31
\end{aligned} \tag{15}$$

For the IDDES model, the length scale (l_{IDDES}) is derived by blending the RANS and LES length scale using the function \tilde{f}_d . Here, the fundamental empirical constant, C_{DES} , is blended using the SST blending function F_1 . The hybrid turbulence model length scale (l_{IDDES}) is given by:

$$\begin{aligned}
l_{IDDES} &= \tilde{f}_d(1 + f_e)l_{RANS} + (1 - \tilde{f}_d)l_{LES} \\
l_{LES} &= C_{DES}\Delta \\
l_{RANS} &= \frac{\sqrt{k}}{\beta^*\omega} \\
C_{DES} &= F_1C_{DES1} + (1 - F_1)C_{DES2}
\end{aligned} \tag{16}$$

The standard sub-grid length scale (Δ) for the LES mode is a function of the nearest wall distance (d) and the maximum edge length of the cell (Δ_{max}). This scale is written as:

$$\Delta = \min(C_w \max[d, \Delta_{max}], \Delta_{max}) \tag{17}$$

Many researchers have observed the standard LES sub-grid length scale based on Δ_{max} suffers from the delayed transition to the LES mode with the DDES based models [20, 21, 27–30]. This delayed flow transition leads to the insufficient flow instability to unlock Kelvin-Helmholtz instabilities in the free shear layer to accelerate the flow transition rapidly in this case. To overcome this problem, the vorticity aligned with a grid line based on Chauvet et al. [22] is used in the current study, which is defined as:

$$\Delta = \min(C_w \max[d, \Delta_{\omega}], \Delta_{\omega}) \tag{18}$$

where,

$$\Delta_{\omega} = \sqrt{(\hat{\mathbf{i}} \cdot \hat{\omega})^2 \Delta_{\eta} \Delta_{\zeta} + (\hat{\mathbf{m}} \cdot \hat{\omega})^2 \Delta_{\zeta} \Delta_{\xi} + (\hat{\mathbf{n}} \cdot \hat{\omega})^2 \Delta_{\xi} \Delta_{\eta}}$$

The blending function \tilde{f}_d is evaluated using the following relations:

$$\begin{aligned}
\tilde{f}_d &= \max((1 - f_{dt}), f_b) \\
f_{dt} &= 1 - \tanh\left[(C_{dt1} r_{dt})^{C_{dt2}}\right] \\
r_{dt} &= \frac{v_t}{\kappa^2 d^2 \sqrt{0.5(S^2 + \Omega^2)}} \frac{1}{Re} \\
f_b &= \min\left(2 \exp(-9\alpha^2), 1.0\right) \\
\alpha &= 0.25 - d/\Delta_{max}
\end{aligned} \tag{19}$$

The elevation function f_e is computed as follow:

$$\begin{aligned}
f_e &= f_{e2} \max((f_{e1} - 1.0), 0.0) \\
f_{e1} &= \begin{cases} 2 \exp(-11.09\alpha^2), & \alpha \geq 0 \\ 2 \exp(-9.0\alpha^2), & \alpha < 0 \end{cases} \\
f_{e2} &= 1 - \max(f_t, f_l) \\
f_t &= \tanh\left(\left(C_t^2 r_{dt}\right)^3\right) \\
f_l &= \tanh\left(\left(C_t^2 r_{dl}\right)^{10}\right) \\
r_{dt} &= \frac{\nu}{\kappa^2 d^2 \sqrt{0.5(S^2 + \Omega^2)}} \frac{1}{Re}
\end{aligned} \tag{20}$$

Additional model constants for IDDES:

$$\begin{aligned}
C_w &= 0.15, & C_{dt1} &= 20, & C_{dt2} &= 3, & \kappa &= 0.41 \\
C_t &= 1.87, & C_l &= 5.0, & C_{DES1} &= 0.78, & C_{DES2} &= 0.61
\end{aligned} \tag{21}$$

B. Fifth-Order WENO Scheme

For the inviscid flux calculation at the interface $i + \frac{1}{2}$, the conservative variables Q_L and Q_R are reconstructed using the fifth order WENO scheme [31, 32]. For example, $(Q_L)_{i+\frac{1}{2}}$ is reconstructed as:

$$(Q_L)_{i+\frac{1}{2}} = \omega_0 q_0 + \omega_1 q_1 + \omega_2 q_2 \tag{22}$$

where,

$$\begin{aligned}
q_0 &= \frac{1}{3}Q_{i-2} - \frac{7}{6}Q_{i-1} + \frac{11}{6}Q_i \\
q_1 &= -\frac{1}{6}Q_{i-1} + \frac{5}{6}Q_i + \frac{1}{3}Q_{i+1} \\
q_2 &= \frac{1}{3}Q_i + \frac{5}{6}Q_{i+1} - \frac{1}{6}Q_{i+2}
\end{aligned} \tag{23}$$

The weight of the stencil is given by

$$\begin{aligned}
\omega_k &= \frac{\alpha_k}{\alpha_0 + \dots + \alpha_{r-1}}, \quad k = 0, \dots, r-1 \text{ with } r = 3 \\
\alpha_k &= \frac{C_k}{(\epsilon + IS_k)^2} \\
C_0 &= 0.1, C_1 = 0.6, C_2 = 0.3
\end{aligned} \tag{24}$$

and the smoothness indicator is calculated by

$$\begin{aligned}
IS_0 &= \frac{13}{12} (Q_{i-2} - 2Q_{i-1} + Q_i)^2 + \frac{1}{4} (Q_{i-2} - 4Q_{i-1} + 3Q_i)^2 \\
IS_1 &= \frac{13}{12} (Q_{i-1} - 2Q_i + Q_{i+1})^2 + \frac{1}{4} (Q_{i-1} - Q_{i+1})^2 \\
IS_2 &= \frac{13}{12} (Q_i - 2Q_{i+1} + Q_{i+2})^2 + \frac{1}{4} (3Q_i - 4Q_{i+1} + Q_{i+2})^2
\end{aligned} \tag{25}$$

ϵ is introduced in the denominator of α_k calculation in Eq. (24) to avoid denominator becoming zero and therefore, it is supposed to be a very small number. The study of Shen et al. [31] found that IS_k oscillates with a small value of ϵ and shifts the weight away from its optimal values in the smooth region. With ϵ significantly higher than IS_k , α_k is less sensitive to the IS_k and ω_k is closed to the C_k . To maintain the sensitivity to shocks in the flow field, ϵ should not be greater than IS_k . Based on the work of Shen et al. [31], the optimal value of ϵ is 10^{-2} for subsonic and transonic flows.

IV. Implicit Time Accurate Flow Solver

The unsteady, compressible RANS equations and the turbulence model are solved in a fully coupled manner using an implicit unfactored Gauss-Seidel line iteration. Their time-dependent form is first control volume integrated and their semi-discretized form is given by:

$$\frac{\partial \mathbf{Q}}{\partial t} = -\frac{1}{\Delta V} \oint_S \mathbf{R}_F \cdot d\mathbf{s} + \mathbf{D} \quad (26)$$

where, \mathbf{R}_F is the net flux vector discretized in the space and \mathbf{D} is the contribution of the source term.

Following Jameson's dual time-stepping method [33], a pseudo temporal term $\partial \mathbf{Q} / \partial \tau$ is added to the left-hand side of Eq. (26). The physical temporal term ($\partial \mathbf{Q} / \partial t$) is discretized using the three-point backward differencing scheme at the physical time levels $n+1$, n and $n-1$. The pseudo temporal term is discretized on two pseudo time steps (i.e. $m+1$ and m) at the same physical time step $n+1$. The final formulation of this dual time-stepping scheme is given by:

$$\left[\left(\frac{1}{\Delta \tau} + \frac{1.5}{\Delta t} \right) I - \left(\frac{\partial \mathbf{RHS}}{\partial \mathbf{Q}} \right)^{n+1, m} \right] \Delta \mathbf{Q}^{n+1, m+1} = \mathbf{RHS}^{n+1, m} - \frac{3\mathbf{Q}^{n+1, m} - 4\mathbf{Q}^n + \mathbf{Q}^{n-1}}{2\Delta t} \quad (27)$$

where,

$$\mathbf{RHS} = -\frac{1}{\Delta V} \oint_S \mathbf{R}_F \cdot d\mathbf{s} + \mathbf{D} \quad (28)$$

Here, the source term jacobian helps to improve the diagonal dominance of the system of equations. In each physical time step, the solution is converged when $\Delta \mathbf{Q}^{n+1, m+1} \rightarrow 0$ and therefore it has no influence on the solution accuracy.

V. Numerical Model for Structure

A. Modal Approach

The equation of motion for N-DOF (degree of freedom) system with mechanical damping and aerodynamic excitation force can be represented in matrix form as:

$$[\mathbf{M}] \{\ddot{\mathbf{X}}\} + [\mathbf{C}] \{\dot{\mathbf{X}}\} + [\mathbf{K}] \{\mathbf{X}\} = \{\mathbf{F}\} \quad (29)$$

where, \mathbf{M} , \mathbf{C} and \mathbf{K} are the mass, structural damping and stiffness matrices, respectively. The aerodynamic excitation force (\mathbf{F}) consists of static pressure and viscous force, given by:

$$\mathbf{F} = - \oint p \cdot \hat{n} dA + \oint \tau_w \cdot \hat{t} dA \quad (30)$$

where, \hat{n} and \hat{t} are the unit normal and tangential vector to the wing surface, respectively. p is the fluid static pressure on the wing surface and τ_w is the fluid wall shear stress acting on the wing surface.

The equations of motion for the damped system, Eq. (29), are decoupled using the mass normalized mode shape ($\tilde{\phi}$) defined as the normal modes divided by square root of the generalized mass ($\sqrt{\phi^T m \phi}$), where m is the elastic body mass. Let, $\{\mathbf{X}\} = [\tilde{\Phi}] \{\mathbf{q}\}$ and premultiplication of Eq. (29) by transpose $[\tilde{\Phi}]^T$ leads to

$$[\tilde{\Phi}]^T [\mathbf{M}] [\tilde{\Phi}] \{\ddot{\mathbf{q}}\} + [\tilde{\Phi}]^T [\mathbf{C}] [\tilde{\Phi}] \{\dot{\mathbf{q}}\} + [\tilde{\Phi}]^T [\mathbf{K}] [\tilde{\Phi}] \{\mathbf{q}\} = [\tilde{\Phi}]^T \{\mathbf{F}\} \quad (31)$$

where, $\{\mathbf{q}\}$ is the principal coordinates vector and $[\tilde{\Phi}] = [\tilde{\phi}_1, \tilde{\phi}_2, \dots, \tilde{\phi}_N]^T$ with N total number of modal coordinates. Using the orthogonality of the system matrices and assuming damping matrix as a linear combination of the mass and stiffness matrices, Eq. (31) is decoupled and the j^{th} equation will have the form as:

$$\ddot{q}_j + 2\zeta_j \omega_j \dot{q}_j + \omega_j^2 q_j = \frac{\tilde{\phi}_j^T}{m_j} F \quad (32)$$

where, ω_j and ζ_j are the natural frequency and the modal damping ratio for mode j . The structural damping of 0.02 is used for all modes [34]. m_j denotes the j^{th} diagonal element of modal mass matrix which will be unity. In the current study, the structural system is reduced to first five mode shapes, since a few bending and torsional frequencies are usually sufficient to determine the flutter. The normalized modal equation can be given by:

$$\ddot{q}_j + 2\zeta_j \left(\frac{\omega_j}{\omega_\alpha} \right) \dot{q}_j + \left(\frac{\omega_j}{\omega_\alpha} \right)^2 q_j = \frac{\tilde{\phi}_j^T}{m_j^*} \cdot F^* \cdot V_f^2 \cdot \frac{b_s^2 L}{\bar{V}} \cdot \bar{m} \quad (33)$$

where, an asterisk denotes the dimensionless quantities and q_j represents the modal displacement of mode j . A flutter speed index, $V_f = \frac{U_\infty}{b_s \omega_\alpha \sqrt{\mu}}$, is an input flutter control parameter. ω_j and ζ_j are the natural frequency and the modal damping ratio of mode j , respectively. The mass ratio, $\mu = \frac{\bar{m}}{V \rho_\infty}$, is the relation between the structural mass and the mass of the equivalent volume of fluid at reference density. L denotes the reference length, \bar{V} represents the conical frustum volume, b_s is the streamwise root semi chord and \bar{m} is the measured wing panel mass. ω_α is the first torsional mode frequency in units rad/s. The nondimensional force is given by $F^* = \frac{F}{\rho_\infty U_\infty^2 L^2}$. For the mass normalized mode shapes, m_j^* should be equal to one. In the present study, the mode shapes of AGARD wing 445.6 weakened model 3 [34] are mass normalized such that m_j^* equals to one in units lbf · in · s² (= 0.112979 kg · m²).

For the time-accurate FSI solver, the Eq. (33) is transformed into the state form as follows:

$$[\mathbf{M}] \frac{\partial \mathbf{S}}{\partial t} + [\mathbf{K}] [\mathbf{S}] = \mathbf{c} \quad (34)$$

where,

$$\mathbf{S} = \begin{pmatrix} q_j \\ \dot{q}_j \end{pmatrix}, \quad \mathbf{M} = [I], \quad \mathbf{K} = \begin{pmatrix} 0 & -1 \\ \left(\frac{\omega_j}{\omega_\alpha} \right)^2 & 2\zeta_j \left(\frac{\omega_j}{\omega_\alpha} \right) \end{pmatrix} \quad (35)$$

$$\mathbf{c} = \begin{pmatrix} 0 \\ \phi_j^T \cdot F^* \cdot V_f^2 \cdot \frac{b_s^2 L}{\bar{V}} \cdot \bar{m} \end{pmatrix} \quad (36)$$

B. Implicit Structural Solver

To solve the structural equations in a fully coupled manner with the CFD solver [9, 35], the decoupled structural modal equations are integrated using the same method as the flow governing equations within each physical time step as:

$$\left(\frac{1}{\Delta\tau} \mathbf{I} + \frac{1.5}{\Delta t} \mathbf{M} + \mathbf{K} \right) \delta \mathbf{S}^{n+1, m+1} = \mathbf{c}^{n+1, m+1} - \mathbf{M} \frac{3\mathbf{S}^{n+1, m} - 4\mathbf{S}^n + \mathbf{S}^{n-1}}{2\Delta t} - \mathbf{K} \mathbf{S}^{n+1, m} \quad (37)$$

In each physical time step, the flow and structural equations are solved iteratively using a pseudo time step until the prescribed convergence criteria are achieved for both solvers. Upon converging to the prescribed level, the fluid-structure interaction solver proceeds to the next physical time step.

VI. Flutter Control Parameters

The flutter occurs with the increasing dynamic pressure to the critical value and beyond [36]. The work of Yates [37, 38] shows the flutter speed and frequency are primarily governed by the density (or mass ratio) and the Mach number. The mass ratio is inversely proportional to the fluid density. The flutter speed index is directly proportional to the free stream fluid velocity and the inverse square root of the free stream fluid density. The change in dynamic pressure at a particular Mach number and angle-of-attack is achieved by changing the free stream fluid density and/or velocity.

Several iterations with varying dynamic pressure are needed to find the neutrally stable point at a particular Mach number and angle-of-attack. In the present study, the flutter speed index and the mass ratio are iterated to find the flutter boundary. In contrast, the nondimensional total pressure, total temperature and the static pressure are kept constant. However, the absolute total pressure, total temperature and the static pressure are allowed to vary, affecting the change in free stream fluid density and velocity at the same Mach number. This leads to the change in the Reynolds number and the dynamic pressure.

VII. Computational Setup

A. AGARD Wing 445.6 Geometry details

In this study, the AGARD Wing 445.6 weakened 3 is used for the flutter analysis at 0° angle-of-attack. The wing model uses symmetry NACA 65A004 airfoil sections along the spanwise direction. The wing has a panel aspect ratio of 1.6525, a panel taper ratio of 0.6576 and 45° of quarter-chord sweptback [34]. The complete wing model details can be found in the ref. [34]. Some of the wing structure details are mentioned in Table 1.

Table 1 AGARD Wing 445.6 weakened 3 model structural details

Measured panel mass (\bar{m}) [kg]	1.8627
Panel span (H) [m]	0.762
Root chord (b_s) [m]	0.559
Tip chord (b_t) [m]	0.3682

B. Computational Grid

The O-mesh topology is used as shown in Fig. 1 as it ensures a highly orthogonal grid near the wall. The far-field boundary extends 55 times the root chord away from the wing. In the spanwise direction, the far-field is about 55 span length of the wing away from the wingtip. The first grid point away from the wall ensures y^+ is below one. The computational grid has the number of grid points of 273 around the airfoil, 84 in the wall-normal direction and 77 points in the spanwise direction.

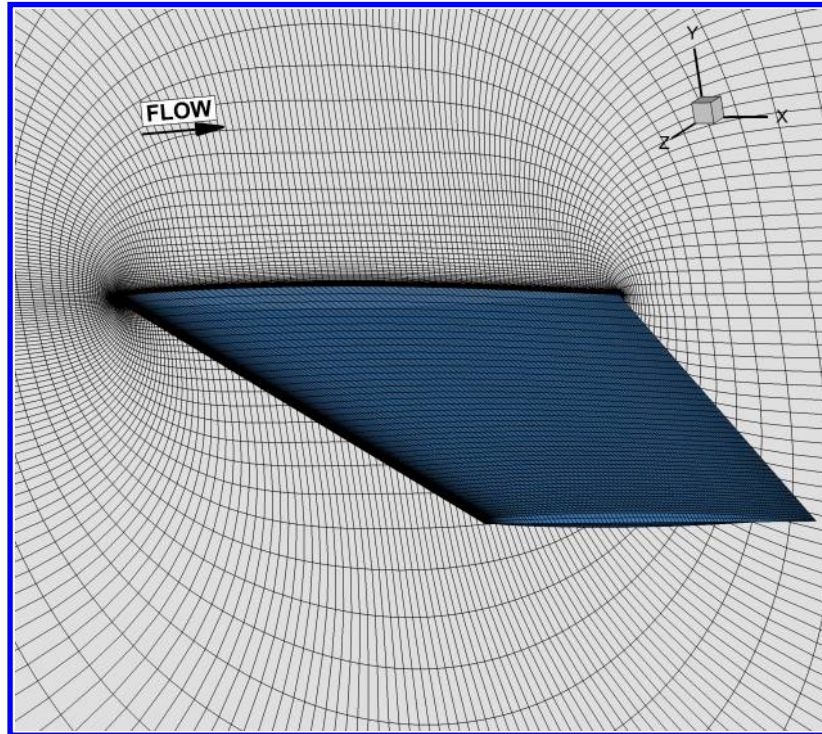


Fig. 1 Computational mesh of 273 x 84 x 77 for AGARD Wing 445.6 weakened 3

C. Numerical Methods

In the present study, the Roe flux difference scheme is used to evaluate the inviscid flux, where the conservative variables at the cell interface are reconstructed with the fifth-order WENO scheme. The fourth-order central differencing

scheme is used to calculate the viscous flux. The transient flow simulation is started from the converged steady-state results with the nondimensional characteristic time step of 0.025 and the pseudo time step based on the CFL number of 1.0. The simulation is carried out for 250 nondimensional characteristic time. In each physical time step, the $L2$ norm of residuals is allowed to reduce by four orders of magnitude, which is usually achieved within 10 to 20 pseudo time steps.

D. Boundary Conditions (BCs)

For the subsonic and transonic flutter calculations, steady-state conditions are used at the inlet. The static pressure is specified at the outlet. In the spanwise direction, the symmetry boundary condition is employed at the wing root. At the far-field in the spanwise direction, the zero gradient boundary condition is applied. At the wall, the no-slip adiabatic moving wall boundary condition is specified. For the supersonic flow, inflow condition with the specified inlet Mach number is applied at the upstream portion of the outer boundary. During the numerical calculations, the Mach number is kept constant and the Reynolds number is varied with the free stream velocity. The nondimensional turbulence kinetic energy (k_∞) and the turbulence specific dissipation rate (ω_∞) at the inlet are calculated based on the Eq. (38) given by:

$$\begin{aligned} k_\infty &= 9 \times 10^{-9} c_\infty^2 \\ \omega_\infty &= 1 \times 10^{-6} \frac{c_\infty^2 \rho_\infty}{\mu_\infty} Re \end{aligned} \quad (38)$$

VIII. Results

A. Mesh Independence Study

The mesh independence study is carried out for the free stream Mach number of 1.14. Three different mesh sizes are used with the total mesh size doubled consecutively as it is very time-consuming for time-marching FSI simulation. The coarse mesh consists a number of grid points of 137 (around airfoil) x 60 (normal to wing surface) x 67 (spanwise). Similarly, the medium and the fine mesh consist of 137 x 84 x 87 and 273 x 84 x 77 grid points. When the mesh is refined, the mode shapes corresponding to the surface mesh coordinates are interpolated by a radial basis function interpolation. Fig. 2 shows the first mode displacement for different meshes at the free stream Mach number of 1.14 and the flutter speed index (V_f) of 0.3776. The predicted generalized displacements for mode-1 are well converged with different meshes. Therefore, fine mesh is chosen for the flutter boundary prediction in this study.

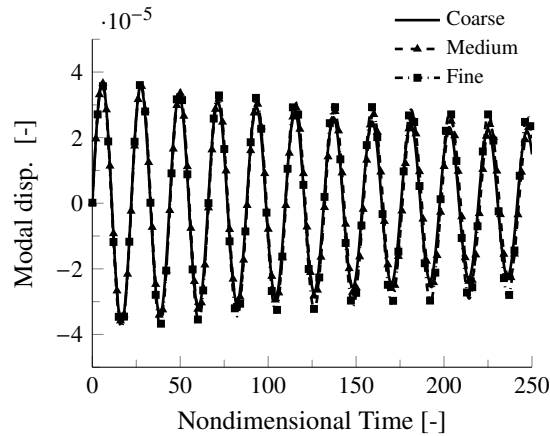


Fig. 2 Mesh independence for $M_\infty = 1.14$, $V_f = 0.3776$

B. Flutter Boundary

Fig. 3 shows the first three mode generalized displacement at the Mach number of 0.96 with varying flutter speed index. At the flutter boundary, as shown in Fig. 3(b), the generalized model displacement exhibits the Limit Cycle Oscillation (LCO). The wing tip generalized displacement damps out below the flutter boundary, Fig. 3(a), and grows

above it, Fig. 3(c). The first two mode generalized displacement contribution is higher as compared to the other remaining modes.

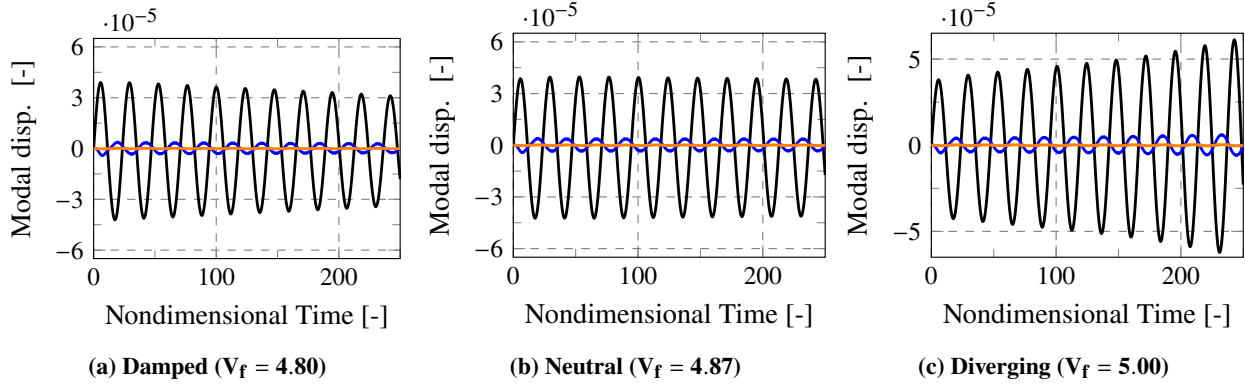


Fig. 3 Generalized displacement of wingtip TE point for $M_\infty = 0.96$

(Mode-1 (—), Mode-2 (—), Mode-3 (—))

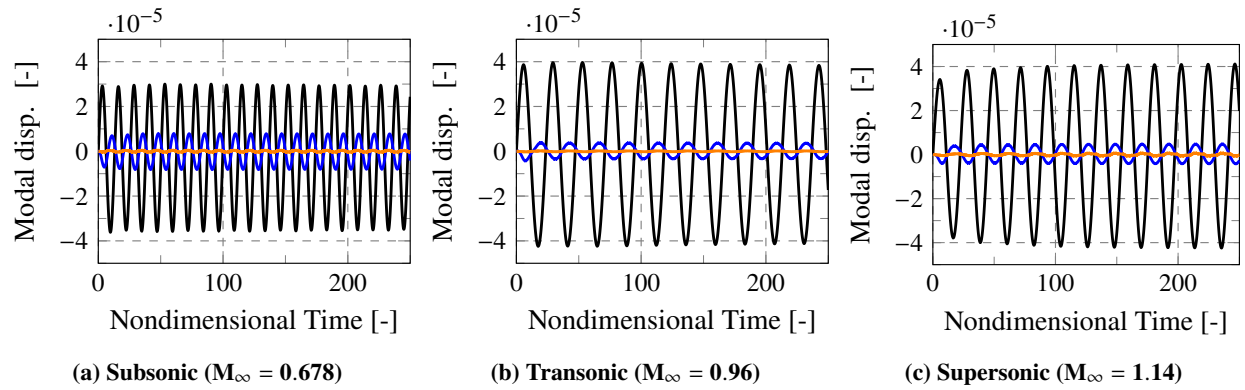


Fig. 4 Generalized displacement of wingtip TE point at/near flutter boundary

(Mode-1 (—), Mode-2 (—), Mode-3 (—))

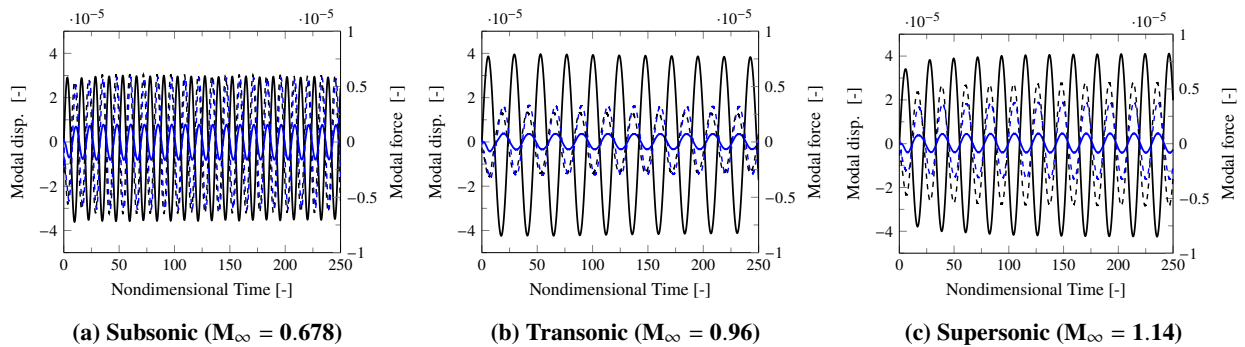


Fig. 5 Generalized displacement and modal force of wingtip TE point at/near flutter boundary

(Mode-1-Disp. (—), Mode-2-Disp. (—), Mode-1-Force (- - -), Mode-2-Force (- - -))

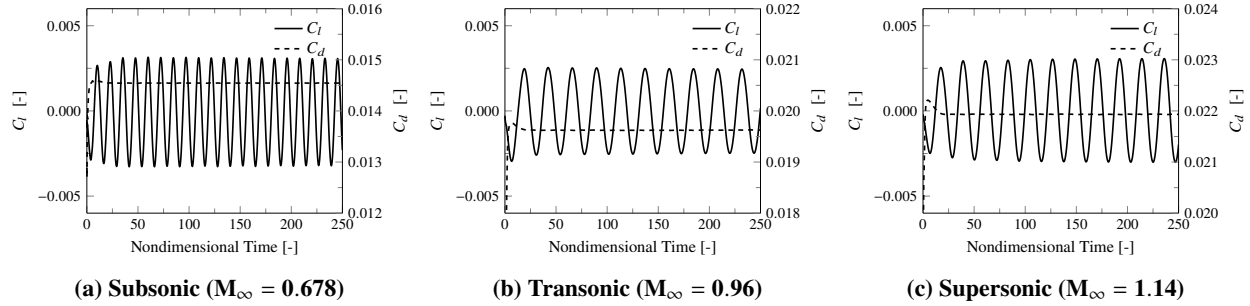


Fig. 6 Lift and drag coefficient at/near flutter boundary

The predicted modal displacements of wingtip TE point are shown in Fig. 4 at the flutter boundary for Mach number of 0.678, 0.96 and 1.14. For the supersonic and transonic flow, the first mode generalized displacement amplitude does not vary much except the reduction in oscillation frequency at the transonic flow. The second mode amplitude is also comparatively smaller. At the subsonic flow, the first mode generalized displacement amplitude decreases in comparison to the transonic and supersonic flow, whereas the second mode displacement amplitude increases. The frequency of oscillation increases at the subsonic flow suggesting the increase in flutter speed index.

Fig. 5 shows the generalized modal displacement and modal force $\frac{\phi_j^T}{m_j} \cdot F^* \cdot V_f^2 \cdot \frac{b_s^2 L}{V} \cdot \bar{m}$ for three different Mach numbers ranging from subsonic to supersonic flow regime. For all Mach numbers, first two modal forces are in phase with the second mode generalized displacement, whereas they have the reverse phase with the first modal displacement. This phenomenon shows that this reverse phase is not responsible for the sonic dip, as observed by Gan et al. [25]. The generalized modal force amplitude at Mach number of 0.678 and 1.14 are very similar, whereas it drops at the Mach number of 0.96.

The predicted lift and drag coefficient for three different Mach numbers at flutter boundary is shown in Fig. 6. The predicted lift coefficient at the transonic flow remains low. The drag coefficient increases from subsonic to supersonic flow due to the wave drag.

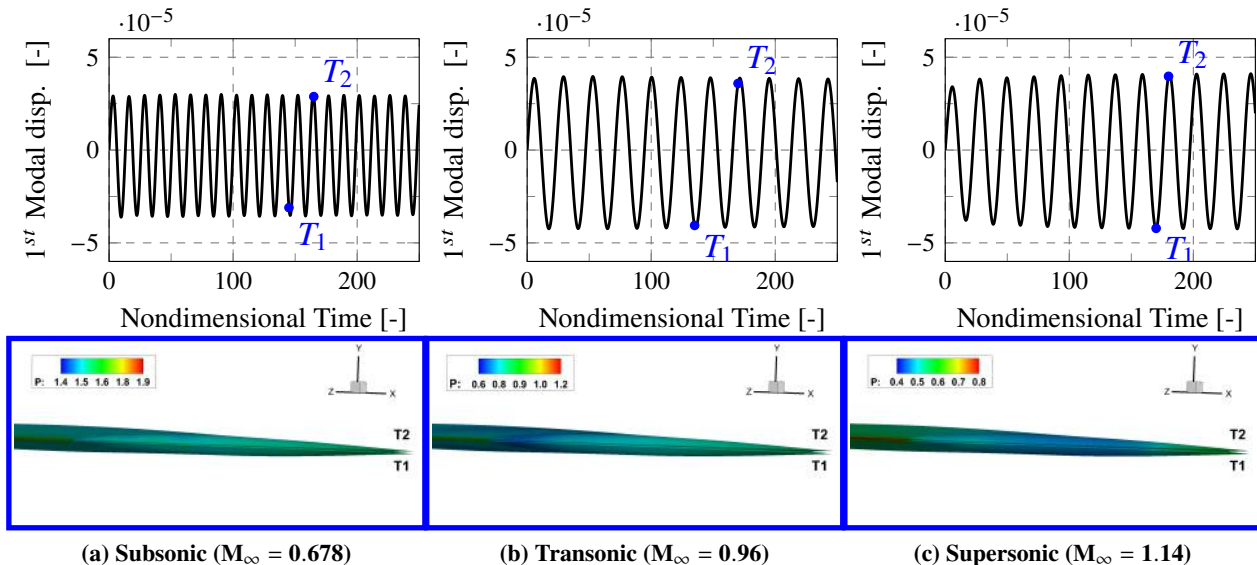


Fig. 7 Generalized displacement of wingtip TE point and wing fluttering

Fig. 7 illustrates the first mode generalized displacement of wingtip TE point and wing fluttering. Two different time steps are marked in the generalized modal displacement plot for which the TE displacements are shown at the bottom. The trailing edge experiences larger amplitude vibration than the leading edge due to the combined effect of generalized bending and torsional force associated with the flutter.

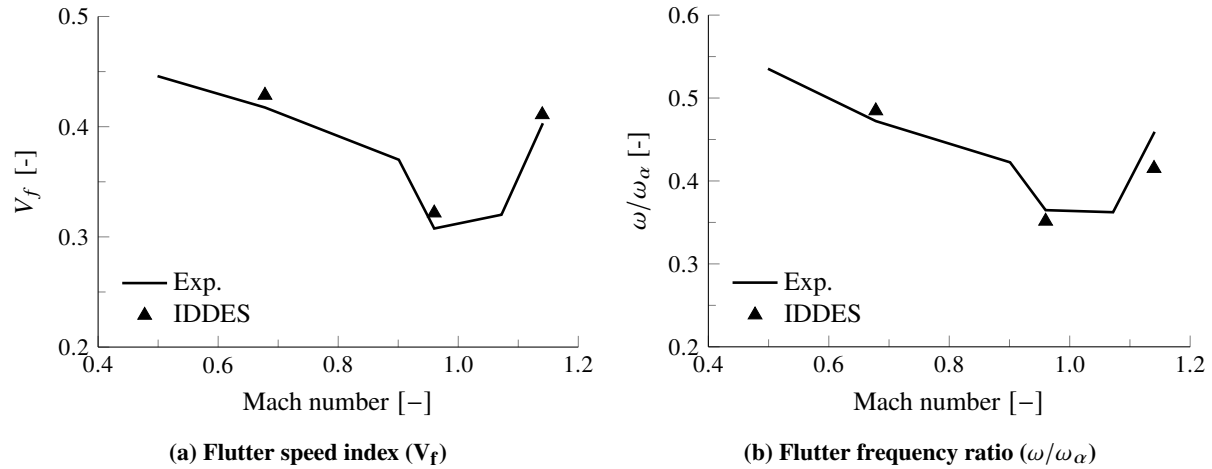


Fig. 8 Flutter boundary

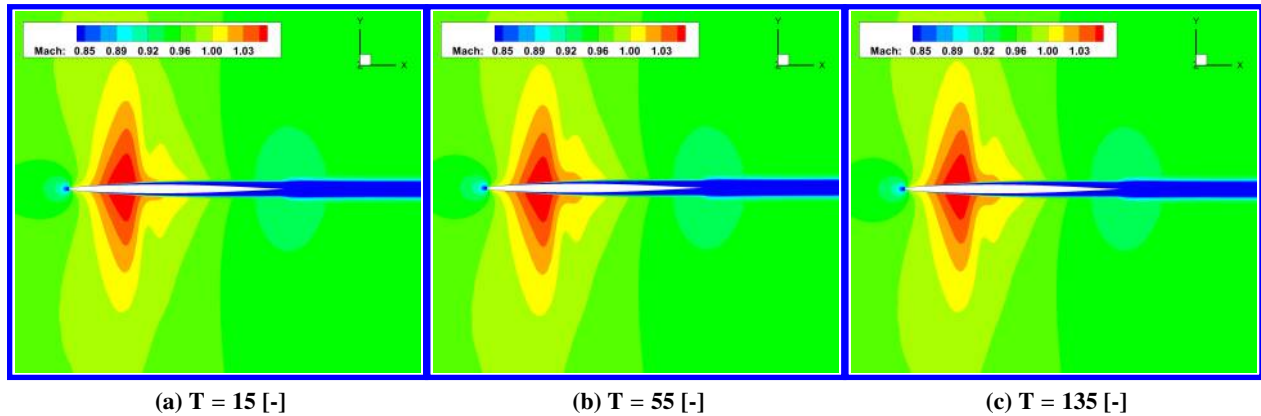


Fig. 9 Instantaneous Mach number contours for $M_\infty = 0.96$ at 92% wing span

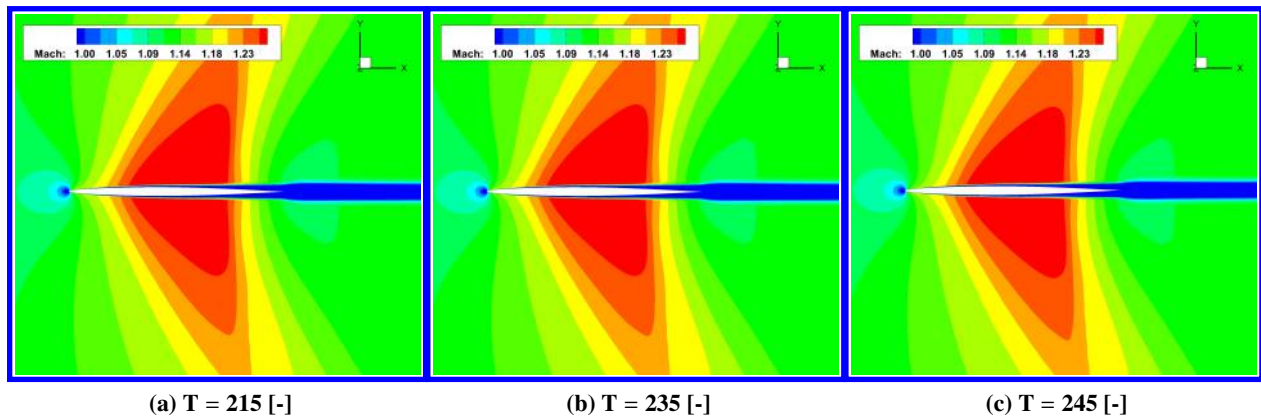


Fig. 10 Instantaneous Mach number contours for $M_\infty = 1.14$ at 92% wing span

The predicted flutter speed index and frequency ratio are compared with the experimental measurements in Fig. 8. Here, the frequency ratio is defined as the ratio of flutter frequency to the first torsional mode natural frequency. The predicted flutter boundary with the hybrid turbulence model is in good agreement with the experiment. The hybrid model predicts the flutter speed index accurately at the supersonic flow in addition to the transonic and subsonic flow.

The flutter frequency ratio is under-predicted by approximately 10% at the Mach number of 1.14 and 4% at the Mach number of 0.96, whereas it is over-predicted by 3% at the Mach number of 0.678.

Fig. 9 shows the instantaneous Mach number contours for $M_\infty = 0.96$ near the wingtip under stable vibration at three different nondimensional time. The supersonic flow region appears on the suction and pressure side of the wing. This supersonic flow region moves back and forth in the flow direction alternatively on the suction and pressure side. This leads to the change in angle-of-attack and the trailing edge movement larger than the leading edge. At $M_\infty = 1.14$ as shown in Fig. 10, the oblique shock wave appears near the trailing edge and its oscillation is larger above the suction and pressure surface. The flow separation is not observed at the subsonic flow and also with the shock-wave boundary layer interaction.

IX. Conclusions

In the present study, the flutter boundary of the AGARD Wing 445.6 is simulated at various Mach numbers using the SST-IDDES with a fully coupled Fluid-Structure Interaction. The Roe approximate Riemann solver with the 5th order WENO reconstructed conservative variables for inviscid flux and the fourth order central differencing scheme for the viscous flux are used to resolve the shock-wave boundary layer interactions. A modal approach with five decoupled modal equations are used to calculate the structural response.

At the transonic and supersonic flow, the viscous forces are predicted more accurately with the hybrid model than its base turbulence model. Therefore, the predicted flutter speed index and frequency ratio are in close agreement with the experimental measurements, in addition to the subsonic flow. The torsional mode displacement contribution decreases at the transonic and supersonic flow. The shock oscillations are larger at the supersonic flow compared to the transonic flow. No flow separation is observed at different Mach numbers.

Acknowledgments

We would like to thank the Center for Computational Science at University of Miami, Coral Gables for providing computational resources.

References

- [1] Edwards, J., and Malone, J., "Current status of computational methods for transonic unsteady aerodynamics and aeroelastic applications," *Computing Systems in Engineering*, Vol. 3, 1992, pp. 545–569.
- [2] Zhang, B., Ding, W., Ji, S., and Zhang, J., "Transonic flutter analysis of an AGARD 445.6 wing in the frequency domain using the Euler method," *Engineering Applications of Computational Fluid Mechanics*, Vol. 10, No. 1, 2016, pp. 243–254. doi:10.1080/19942060.2016.1152200, URL <https://doi.org/10.1080/19942060.2016.1152200>.
- [3] Schuster, D. M., Liu, D. D., and Huttshell, L. J., "Computational aeroelasticity: Success, progress, challenge," *Journal of Aircraft*, Vol. 40, No. 5, 2003, pp. 843–856. doi:10.2514/2.6875, URL <https://doi.org/10.2514/2.6875>.
- [4] Lee-rausch, E., and Batina, J., "Calculation of AGARD wing 445.6 flutter using Navier-Stokes aerodynamics," Tech. rep., Aug. 1993.
- [5] Cunningham, H. J., Batina, J. T., and Bennett, R. M., "Modern wing flutter analysis by computational fluid dynamics methods," *Journal of Aircraft*, Vol. 25, No. 10, 1988, pp. 962–968. doi:10.2514/3.45686, URL <https://doi.org/10.2514/3.45686>.
- [6] Rausch, R. D., Batina, J. T., and Yang, H. T. Y., "Three-dimensional time-marching aeroelastic analyses using an unstructured-grid Euler method," *AIAA Journal*, Vol. 31, No. 9, 1993, pp. 1626–1633. doi:10.2514/3.11824, URL <https://doi.org/10.2514/3.11824>.
- [7] Elizabeth M., L.-R., and John T., B., *Wing flutter boundary prediction using unsteady Euler aerodynamic method*, 1993. doi:10.2514/6.1993-1422, URL <https://arc.aiaa.org/doi/abs/10.2514/6.1993-1422>.
- [8] Opgenoord, M., "Transonic flutter prediction and aeroelastic tailoring for next-generation transport aircraft," Ph.D. thesis, 08 2018.
- [9] Chen, X., Zha, G.-C., and Yang, M.-T., "Numerical simulation of 3-D wing flutter with fully coupled fluid-structural interaction," *Computers & Fluids*, Vol. 36, No. 5, 2007, pp. 856 – 867. doi:<https://doi.org/10.1016/j.compfluid.2006.08.005>, URL <http://www.sciencedirect.com/science/article/pii/S0045793006001034>.

- [10] Spalart, P. R., Jou, W.-H., Strelets, M., and Allmaras, S., “Comments on the feasibility of LES for wings, and on a hybrid RANS/LES approach,” 1997.
- [11] Menter, F., and Kuntz, M., *Adaptation of eddy-viscosity turbulence models to unsteady separated flow behind vehicles*, 2004, Vol. 19, pp. 339–352. doi:10.1007/978-3-540-44419-0_30.
- [12] Spalart, P. R., Deck, S., Shur, M. L., Squires, K. D., Strelets, M. K., and Travin, A. K., “A new version of detached-eddy simulation, resistant to ambiguous grid densities,” *Theoretical and Computational Fluid Dynamics*, Vol. 20, No. 3, 2006, p. 181. doi:10.1007/s00162-006-0015-0, URL <https://doi.org/10.1007/s00162-006-0015-0>.
- [13] Strelets, M., *Detached eddy simulation of massively separated flows*, 2001. doi:10.2514/6.2001-879, URL <https://arc.aiaa.org/doi/abs/10.2514/6.2001-879>.
- [14] Menter, F. R., Kuntz, M., and Langtry, R., “Ten years of industrial experience with the SST turbulence model,” *Turbulence Heat and Mass Transfer*, Vol. 4, 2003, pp. 625–632.
- [15] Nikitin, N. V., Nicoud, F., Wasistho, B., Squires, K. D., and Spalart, P. R., “An approach to wall modeling in large-eddy simulations,” *Physics of Fluids*, Vol. 12, No. 7, 2000, pp. 1629–1632. doi:10.1063/1.870414, URL <https://doi.org/10.1063/1.870414>.
- [16] Shur, M. L., Spalart, P. R., Strelets, M. K., and Travin, A. K., “A hybrid RANS-LES approach with delayed-DES and wall-modelled LES capabilities,” *International Journal of Heat and Fluid Flow*, Vol. 29, No. 6, 2008, pp. 1638 – 1649. URL <http://www.sciencedirect.com/science/article/pii/S0142727X08001203>.
- [17] Gritskevich, M., Garbaruk, A., Schütze, J., and Menter, F., “Development of DDES and IDDES formulations for the $k - \omega$ shear stress transport model,” *Flow, Turbulence and Combustion*, Vol. 88, 2012. doi:10.1007/s10494-011-9378-4.
- [18] Ashton, N., “Development, Implementation and Testing of an Alternative DDES Formulation Based on Elliptic Relaxation,” phdthesis, The University of Manchester, Aug. 2012.
- [19] Ashton, N., Revell, A., Prosser, R., and Uribe, J., “Development of an Alternative Delayed Detached-Eddy Simulation Formulation Based on Elliptic Relaxation,” *AIAA Journal*, Vol. 51, No. 2, 2013, pp. 513–519. doi:10.2514/1.J051808.
- [20] Probst, A., Schwaborn, D., Garbaruk, A., Guseva, E., Shur, M., Strelets, M., and Travin, A., “Evaluation of grey area mitigation tools within zonal and non-zonal RANS-LES approaches in flows with pressure induced separation,” *International Journal of Heat and Fluid Flow*, Vol. 68, 2017, pp. 237 – 247. doi:10.1016/j.ijheatfluidflow.2017.08.008.
- [21] Fuchs, M., Mockett, C., Sesterhenn, J., and Thiele, F., *The grey-area improved σ -DDES approach: formulation review and application to complex test cases*, 2020, pp. 119–130. doi:10.1007/978-3-030-27607-2_9.
- [22] Chauvet, N., Deck, S., and Jacquin, L., “Zonal detached eddy simulation of a controlled propulsive jet,” *AIAA Journal*, Vol. 45, No. 10, 2007, pp. 2458–2473. doi:10.2514/1.28562.
- [23] Chen, X., Wang, B., and Zha, G., “Delayed detached eddy simulation of 3-D wing flutter with fully coupled fluid-structural interaction,” *48th AIAA Aerospace Sciences Meeting Including the New Horizons Forum and Aerospace Exposition*, 2010. doi:10.2514/6.2010-53.
- [24] Im, H., Chen, X., and Zha, G., “Prediction of a Supersonic Wing Flutter Boundary Using a High Fidelity Detached Eddy Simulation,” 2012. doi:10.2514/6.2012-39.
- [25] Gan, J., Im, H., Chen, X., Zha, G., and Pasiliao, C. L., “Delayed detached Eddy simulation of wing flutter boundary using high order schemes,” *Journal of Fluids and Structures*, Vol. 71, 2017, pp. 199 – 216. doi:https://doi.org/10.1016/j.jfluidstructs.2017.03.002, URL <http://www.sciencedirect.com/science/article/pii/S088997461630278X>.
- [26] Šekutkovski, B., Kosti, I., Simonovi, A., Cardiff, P., and Jazarevi, V., “Three-dimensional fluidstructure interaction simulation with a hybrid RANSLES turbulence model for applications in transonic flow domain,” *Aerospace Science and Technology*, Vol. 49, 2016, pp. 1 – 16. doi:https://doi.org/10.1016/j.ast.2015.11.028, URL <http://www.sciencedirect.com/science/article/pii/S1270963815003727>.
- [27] Patel, P., and Zha, G., “Improved delayed detached eddy simulation of separated flow,” *AIAA Aviation 2020 Forum*, 2020. doi:10.2514/6.2020-3013, URL <https://arc.aiaa.org/doi/abs/10.2514/6.2020-3013>.
- [28] Guseva, E., Garbaruk, A., and Strelets, M., “Assessment of Delayed DES and Improved Delayed DES combined with a shear-layer-adapted subgrid length-scale in separated flows,” *Flow, Turbulence and Combustion*, Vol. 98, 2016. doi:10.1007/s10494-016-9769-7.

- [29] Kiris, C. C., Stich, D., Housman, J. A., Kocheemoolayil, J. G., Barad, M. F., and Cadieux, F., *Application of Lattice Boltzmann and Navier-Stokes methods to NASAs wall mounted hump*, 2018. doi:10.2514/6.2018-3855, AIAA 2018-3855.
- [30] Patel, P. C., “RANS/LES hybrid turbulence simulation of axial compressor non-synchronous vibration,” Ph.D. thesis, University of Miami, Aug. 2020.
- [31] Shen, Y., Zha, G., and Wang, B., “Improvement of stability and accuracy for weighted essentially nonoscillatory scheme,” *AIAA Journal*, Vol. 47, No. 2, 2009, pp. 331–344. doi:10.2514/1.37697, URL <https://doi.org/10.2514/1.37697>.
- [32] Shen, Y., and Zha, G., “Improvement of the WENO scheme smoothness estimator,” *International Journal for Numerical Methods in Fluids*, Vol. 64, No. 6, 2009, pp. 653–675. doi:10.1002/flid.2168, URL <https://onlinelibrary.wiley.com/doi/abs/10.1002/flid.2168>.
- [33] Jameson, A., “Time dependent calculations using multigrid, with applications to unsteady flows past airfoils and wings,” Fluid Dynamics and Co-located Conferences, American Institute of Aeronautics and Astronautics, 1991. doi:10.2514/6.1991-1596, URL <https://doi.org/10.2514/6.1991-1596>.
- [34] Yates, E., *AGARD standard aeroelastic configurations for dynamic response. Candidate configuration I.-wing 445.6*, 1987. NASA-TM-100492.
- [35] Chen, X., and Zha, G.-C., “Fully coupled fluid-structural interactions using an efficient high resolution upwind scheme,” *Journal of Fluids and Structures*, Vol. 20, No. 8, 2005, pp. 1105 – 1125. doi:<https://doi.org/10.1016/j.jfluidstructs.2005.02.011>, URL <http://www.sciencedirect.com/science/article/pii/S0889974605000496>.
- [36] Parker, G., “Dynamic aeroelastic analysis of wing/store configurations,” Ph.D. thesis, Air Force Institute of Technology, Dec. 2005.
- [37] Yates, E., *Some effects of variations in density and aerodynamic parameters on the calculated flutter characteristics of finite-span swept and unswept wings at subsonic and supersonic speeds*, NASA technical memorandum, National Aeronautics and Space Administration, 1960. NASA-TM-X-182.
- [38] Yates, E., *Subsonic and supersonic flutter analysis of a highly tapered swept-wing planform, including effects of density variation and finite wing thickness, and comparison with experiments*, NASA technical memorandum, 1967. NASA-TN-D-4230.